Radiometric and Spectral Performance and Calibration of the GHz Bands of EOS MLS

Robert F. Jarnot, Vincent S. Perun, and Michael J. Schwartz

***Abstract*—This paper describes radiometric performance and prelaunch radiometric and spectral calibrations of the GHz component of the Microwave Limb Sounder (MLS) experiment on NASA's Aura spacecraft. Estimated systematic scaling uncertainties (3σ) on limb port radiances are $\sim$0.5% from radiometric calibration and $\sim$0.5% to $\sim$1% from spectral calibrations. Operational noise performance is consistent with prelaunch expectations, and in-orbit measurements to date indicate no changes in noise characteristics, and no observable calibration drifts. Spectral baseline has remained stable to $\sim$20 mK since launch. Refinements to calibrations based on in-flight data are discussed, and radiometric calibration algorithms are described.**

***Index Terms*—Calibration, GHz, limb sounding, microwave, submillimeter wave.**

NOMENCLATURE

ΔI	Noise on a calibrated measurement.
ϵ	Calibration target emissivity.
η_r^X	Transmission through switching mirror port X in band r.
τ	Data integration time.
B	Noise bandwidth.
C_i^X	Raw data "counts" in channel i for view to scene X.
C_i^O	Raw data counts for channel i with no signal at the spectrometer input.
DACS	128-channel digital autocorrelator spectrometer.
FB11	11-channel filterbank spectrometer.
FB25	25-channel filterbank spectrometer.
g_i	Radiometric gain (Counts/K) of channel i.
GHz	Gigahertz, 10^9 Hz.
h	Planck's constant.
k	Boltzmann's constant.
Level 1:	Software that converts raw instrument data into calibrated form.
Level 2:	Software that transforms Level 1 output into retrieved atmospheric quantities/profiles.
MAF	Major frame, nominally 148 MIFs, comprising a complete limb scan/calibration cycle.
MHz	Megahertz, 10^6 Hz.
MIF	Minor frame, nominally 1/6 s, during which science data are integrated.
ms	Millisecond $(10^{-3}\ \mathrm{s})$.
$\dot{P}_i^X$	Radiance in channel i from port X.
T	Physical temperature, in Kelvin.
T_{sys}	System temperature, the combination of scene brightness and radiometer noise in temperature units. This is a measure of measurement precision when used in conjunction with the Radiometer Equation.

I. INTRODUCTION

THE Earth Observing System (EOS) Microwave Limb Sounder (MLS) on Aura is a follow-on to the successful MLS instrument on the Upper Atmosphere Research Satellite (UARS) [1]. It measures thermal emission from the Earth's atmospheric limb to infer vertical profiles of minor constituents of interest to improving understanding atmospheric chemistry and dynamics in regions spanning the upper troposphere to mesosphere. Four radiometers in the GHz module, R1 through R4, measure bands centered near 118, 190, 240, and 640 GHz (there are two 118-GHz bands to provide redundancy for critical pressure and temperature measurements). Twenty-one nominally identical 25-channel filterbanks (FB25), each with $\sim$1.3-GHz spectral coverage, analyze the signals from these radiometers. An additional five 11-channel filterbanks with narrower ($\sim$200 MHz) analysis bandwidth target specific features in the 190- and 640-GHz radiometer passbands. The 25-channel filterbanks have a "zoom" structure with 96-MHz wide channels at the edges (channels 1 and 25), progressively narrowing down to 6-MHz resolution at band center (channel 13). The 11-channel filterbanks implement just the center 11 channels of an FB25. Four narrow-band (10 MHz) digital autocorrelator spectrometers (DACS) are used to analyze high-altitude O_2, O_3, CO, and H_2O signals. A more detailed description of the instrument, its operation, mission, and measurements, is given in a companion paper in this issue [2]. In this paper, we describe in-orbit radiometric performance, the radiometric and spectral calibration of the GHz portion of Aura MLS, and the algorithms used to convert raw data into calibrated radiances. Additional companion papers in this issue describe the field-of-view (FOV) calibrations of the GHz radiometers [3] and the THz portion of MLS together with all aspects of its calibration [4].

Compared to its predecessor, the current instrument implements twice as many radiometers, each with substantially greater measurement bandwidth and spanning a considerably larger overall frequency range. The number of measurement channels, a partial indicator of the magnitude of the calibration effort, is increased by an order of magnitude, and the instrument

---

Manuscript received April 27, 2005; revised September 20, 2005. This work was done at the Jet Propulsion Laboratory, California Institute of Technology, Pasadena, under contract to the U.S. National Aeronautics and Space Administration.

The authors are with the Jet Propulsion Laboratory, California Institute of Technology, Pasadena, CA 91109-8099 USA (e-mail: Robert.F.Jarnot@jpl.nasa.gov).

Digital Object Identifier 10.1109/TGRS.2005.863714

data rate by two orders of magnitude. The calibration techniques described in this paper evolved from those employed on UARS MLS [5], but with significant enhancements in data quality and measurement efficiency to support the order of magnitude increase in the quantity of calibration data processed and used in higher levels of data processing.

In this paper, we outline operation of the instrument and provide details on its radiometric and spectral calibration, and of the radiometric calibration algorithms. Primary objectives include end-to-end verification and calibration of the instrument signal paths, and radiometric and spectral calibrations each with better than 1% uncertainty. Comprehensive material describing these measurements is available from the authors.

A. Radiance Units

The MLS radiometers are heterodyne systems which receive power $h\nu/\{\exp(h\nu/kT) - 1\}$ per unit frequency range when viewing a blackbody source at temperature T which completely fills their FOV, where ν is frequency, h is Planck's constant, and k is Boltzmann's constant. MLS signals originate thermally, and it is convenient to measure radiant power per unit bandwidth, $\dot{P}_\nu$, in units of temperature so that the measure converges to the absolute temperature, T, in the long wave (Rayleigh-Jeans) limit where $h\nu \ll kT$ and classical statistical mechanics applies. For the blackbody, this is

$$\overset{\bullet}{P}_\nu = \frac{h\nu}{k\left\{\exp\left(\frac{h\nu}{kT}\right) - 1\right\}}. \qquad (1)$$

For the range of frequencies and scene temperatures (150–300 K) observed by MLS the relationship between P_ν and scene temperature is essentially linear, with a small frequency-dependent offset ranging from ~3 to ~15 K (for the 118–640-GHz radiometers, respectively) [6]. All measured signals (radiances) in this paper are thus presented in intuitive units of Kelvin, and we also choose to express instrument noise in the same units, corresponding to the statistical noise from observation of a scene at that radiative temperature.

B. Measurement Sequence and Radiance Calibration Process

Aura MLS radiance observations consist of a continuous sequence of 161-ms data integrations separated by 5-ms dead time. The 166-ms integration/dead time period is referred to as a minor frame (MIF). MIFs are grouped into major frames (MAF), each of which contains 148 MIFs (24.7 s), the first 120 of which are used to view the atmospheric limb. The remaining MIFs are used for viewing cold space (12 MIFs) and one of two radiometric calibration targets (six MIFs). A switching mirror common to all GHz radiometers is used to direct the receiver FOVs to one of four ports (limb, space, ambient, or cooled calibration target). Ten MIFs of each MAF are used to step and settle the switching mirror, and measurements are made in a total-power (nonchopped) mode. The ambient target is near room temperature, and the other target is cooled passively by ~ 40 °C. Only one target is viewed routinely as part of the radiometric calibration process, but both targets have been viewed using special switching sequences in order to verify linearity and provide more details of standing waves. Details of atmospheric scanning are provided in [2].

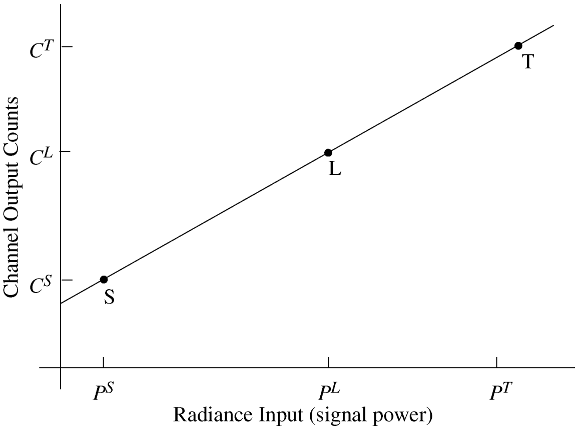

Fig. 1. This figure indicates the linear relationship between measured radiance P and channel output C. S and T indicate views to cold space and an ambient calibration target, and L indicates a view to the Earth's limb via the main antenna.

The Aura MLS radiance calibration process and algorithms are based on the UARS MLS implementation. Since all GHz radiometers share a common switching mirror, all channels are radiometrically calibrated simultaneously. Ideally we can represent the output of a single measurement channel by the linear transfer function shown in Fig. 1.

II. RADIOMETRIC CALIBRATION ALGORITHMS

The software which converts raw data into calibrated radiances is called Level 1 data processing, and its radiometric calibration algorithms are described in detail in [6]. The switching mirror FOVs to the space, target, and limb ports are partially restricted by the apertures of the corresponding ports of the cavity in which it is located. Representing the transmission through port X by η^{MX}, the output of a filter channel, C^X, is given by

$$\begin{aligned}
C_i^L &= g_i\left(\eta_r^{ML}\overset{\bullet}{P}_i^{A} + \left(1 - \eta_r^{ML}\right)\overset{\bullet}{P}_r^{BL}\right) + C_i^O\\
C_i^T &= g_i\left(\eta_r^{MT}\overset{\bullet}{P}_r^{T} + \left(1 - \eta_r^{MT}\right)\overset{\bullet}{P}_r^{BT}\right) + C_i^O\\
C_i^S &= g_i\left(\eta_r^{MS}\overset{\bullet}{P}_r^{S} + \left(1 - \eta_r^{MS}\right)\overset{\bullet}{P}_r^{BS}\right) + C_i^O \qquad (2)
\end{aligned}$$

where C_i^X are the outputs of channel i for the three switching mirror positions (X) used operationally, and g_i is the radiometric gain of channel i (expressed in counts per Kelvin of signal brightness). The digitizer offset counts for channel i are indicated by C_i^O, set by a combination of the electronics offsets in the measurement system, and the noise contribution of the receiver electronics (system temperature). Baffle transmissions η^{MX} are determined for each radiometer as part of the FOV calibration activity, and baffle radiances $\dot{P}^{BX}$ determined from engineering telemetry. $\dot{P}_r^X$, where X is one of A, T or S, are the brightness temperatures seen at through the antenna, target and space view ports respectively. Subscript r indicates the radiometer dependence of calibration parameters and radiances.

The first significant step in the radiance calibration process is to estimate radiometric gain, $\hat{g}_i$, at the time of each limb-viewing MIF

$$\hat{g}_i = \frac{\left(\widehat{C}^T - \widehat{C}^S\right)}{\left(\eta^{MT}\epsilon P^{\bullet T} - \eta^{MS}P^{\bullet S} + (1-\eta^{MT})P^{\bullet BT} - (1-\eta^{MS})P^{\bullet BS}\right)} \quad (3)$$

where subscripts i and r on the right-hand side of the equation have been dropped for clarity. The emissivity of the calibration target, ϵ, is discussed later. Radiometric calibrations are performed on MAF-sized chunks of limb data. The estimates of target and space view signals at the time of each limb view in the MAF being calibrated, $\widehat{C}^T$ and $\widehat{C}^S$, are obtained by quadratic interpolation of the space and target view data from six groups of calibration views, three on either side of the group of limb data being processed. Note that the *difference* between interpolated target and space counts is used in this expression, removing the need to estimate C_i^O in (2), but requiring that any drifts in this offset be well fit by the quadratic interpolators over timescales of ~3 min. Adequate stability is obtained through appropriate choice of electronic components, careful design of electronic subsystems, and good thermal stability. Prior experience with UARS MLS led us to design for temperature stability better than 0.01 K per 100 s in the signal processing electronics. This performance is achieved in orbit, and drift characteristics have been acceptably small in both magnitude and derivative.

After radiometric gain has been determined, the atmospheric radiance entering the limb port from the external telescope, $\dot{P}_i^L$, is determined from

$$\overset{\bullet}{P}{}_i^L = \frac{1}{\eta_r^{ML}} \left(\frac{C_i^L - \widehat{C}_i^S(L)}{\hat{g}_i(L)} + \eta_r^{MS} \overset{\bullet}{P}{}_r^S - \left(1-\eta_r^{ML}\right) \overset{\bullet}{P}{}_r^{BL} + \left(1-\eta_r^{MS}\right) \overset{\bullet}{P}{}_r^{BS} \right) \quad (4)$$

where $\widehat{C}_i^S(L)$ is the interpolated value of the space counts at the time of the limb view. In addition to the atmospheric radiance, there are significant additional radiance components reaching the switching mirror limb port, in particular emission from the antenna surfaces, and scattered/diffracted radiation from the spacecraft and the Earth. These components are included in the limb port radiances estimated by the Level 1 software [3].

1) Antenna Baseline Correction: Views to space via the space and limb ports (with the antenna viewing well above the Earth's limb) differ by up to ~10 K in offset, and ~0.5 K in spectral structure. The spectrally flat component arises mostly from thermal emission, scattering, and diffraction at the antenna reflectors. The smaller spectrally varying components are from standing waves and from frequency dependence of the illumination and diffraction sidelobes. Level 1 software makes a first order correction for some of these radiance differences [3], but significant residual errors remain. Two approaches are used in Level 1 to address these remaining residuals.

1) Spectrally averaged (dc) offsets are determined on a MAF-by-MAF basis independently for each band by averaging all limb observations above a tangent height of 85 km in channels which have negligible predicted atmospheric radiances.
2) Spectrally varying (ac) offsets are periodically measured by viewing the Earth's limb at tangent points well above those at which atmospheric signals are present.

A separate dc offset estimate is provided in the Level 1 radiance files for each measurement band, and also for each of the 12 individual ~500-MHz wide filter channels in the 118- and 240-GHz radiometers.

Special measurement sequences run during instrument activation confirmed the stability and lack of scan dependence of the ac baseline, down to the few tens of mK level. The ac baseline is currently reported in the Level 1 radiance file as a static quantity for all filter channels based on the data from these extended high tangent point scans, but investigations are underway to determine if spectral baseline can be measured on a daily basis to accommodate slow changes which arise as a result of seasonal changes in solar β angle (as was done for UARS MLS).

2) Calibration Targets: Emissivities of the calibration targets were measured prior to launch using a set of swept RF sources and broadband receivers. The return signal from the targets was compared to that from a reference reflector over the full range of angles and orientations seen by the radiometers. This provided verification that no harmful diffractive effects were created by the grooved surface structure of the microwave absorbers. Return loss was better than 30 dB over the full frequency range spanned by the GHz receivers. During routine operation only one of the two GHz calibration targets is used as a radiometric reference every MAF, and we currently use the one attached to the radiative cooler. This is because of a prelaunch prediction that the surface of the other target would see a brief indirect reflection of sunlight from the antenna structure as the instrument came into solar illumination. Use of the cooled target gives rise to a small difference between the temperature of the target reported in engineering telemetry, and the surface of the target (which "sees" an environment ~40 K warmer). Tests run during instrument activation showed that the radiative temperature of the cooled target was between 0.5 and 0.6 K higher than that reported in telemetry. The range arises from the varying skin depth of the target surface absorbing material, the largest discrepancy arising in the highest frequency radiometer. This temperature "error" is corrected in the Level 1 processing algorithms.

The finite reflectivity of the calibration targets gives rise to small standing waves, of order a few tenths of a Kelvin, in each band. We have no way of measuring these separately for each target in flight, leading to an uncorrectable radiometric gain error component of up to ~0.1%.

3) Precision: The noise on a time series of data from an individual channel, ΔT, is commonly represented by

$$\Delta T = T_{\text{sys}} \sqrt{\frac{1}{B\tau} + \left(\frac{\Delta G}{G}\right)^2} \quad (5)$$

where T_{sys} is the combination of receiver system temperature and scene radiance, B the predetection noise bandwidth, and τ

TABLE I
IN-ORBIT SPECTRALLY VARYING NOISE IN EOS MLS GIGAHERTZ BANDS FOR 1/6-S INTEGRATION TIME. $\Delta I_{\min}$ DATA ARE FROM LONG (MULTIORBIT) CHARACTERIZATION TESTS

Band	T_{sys}	$\Delta I_{6\,\mathrm{MHz}}$	$\Delta I_{96\,\mathrm{MHz}}$	$\Delta I_{\min}$
R1A	1200 K	.2 K	0.35 K	0.02 K
R1B	1400 K	1.3 K	0.40 K	0.02 K
R1BWF	1200 K	ΔI_{500} = 0.23 K		0.02 K
R2	1000 K	3.2 K	0.9 K	0.02 K
R3	1400 K	4 K	1 K	0.02 K
R3WF	1400 K	ΔI_{500} = 0.4 K		0.02 K
R4	4200 K	10 K	3 K	0.1 K

TABLE II
SYSTEMATIC ERROR BUDGET FOR LIMB PORT RADIANCES, EXPRESSED AS A PERCENTAGE OF REPORTED LIMB RADIANCE

Calibration Target temperature uncertainty	0.1%
Standing Waves	0.1%
Switching Mirror Baffle uncertainty	0.15%
End-to-end linearity	0.1%
Total	0.45%

the postdetection integration time. The $1/B\tau$ component, commonly referred to as radiometer noise [7], is uncorrelated between channels. Gain variations along the signal paths, indicated by the $\Delta G/G$ term, provide a correlated source of noise between all channels of a given radiometer. The radiometers' contribution to T_{sys} is determined once per MAF from the space view calibration data. The gain variation component is determined periodically from Fourier analysis of channel time-series data taken with the instrument staring at either cold space or an internal calibration target for an extended period. We have found the gain variation behavior to be stable in the long-term, with good agreement between prelaunch thermal-vacuum test data and results obtained in orbit.

Level 1 software provides an estimate of the spectrally varying (uncorrelated) noise for each calibrated limb radiance based on the radiometer noise component of (5), with small additional contributions to account for noise on the reference measurements [6]. The gain variation contribution to precision is monitored routinely by determining the ratio of observed variance of each group of cold space measurements to that predicted by radiometer noise alone. Gain variation characteristics have remained stable for the mission to date, allowing Level 1 to provide a static estimate of correlated noise to higher levels of data processing.

A. Radiometric Performance and Accuracy

Table I shows the measured in-orbit spectrally varying noise for all GHz bands expressed as T_{sys} and ΔI (time-series noise) in 6-, 96-, and 500-MHz bandwidth filter channels for single data integrations (1/6 s). The ΔI values are double-sideband quantities except for the 118-GHz R1 radiometers which are single-sideband MMIC implementations. The $\Delta I_{\min}$ column indicates the levels down to which signals are required to integrate, and it was determined that this requirement was met by differencing sets of spectra measured when viewing space via the main antenna for an extended period. Long data integrations, such as are required for measuring BrO, are expected to indicate substantially better $\Delta I_{\min}$ performance than indicated in the table. All spectrally varying noise requirements are met.

Spectrally averaged noise is expressed as a multiplier on T_{sys}, and is band-dependent, ranging from $\sim 2 \times 10^{-4} \times T_{\mathrm{sys}}$ to $\sim 3.5 \times 10^{-4} \times T_{\mathrm{sys}}$, meeting requirements.

The primary sources of systematic radiance errors are summarized in Table II, expressed as a percentage of the limb port radiance reported by Level 1 software. Errors for signals close to radiometric balance have negligible standing wave error contribution due to the baseline corrections at Level 1. Linearity errors are a maximum for signals midway between cold space and calibration target in radiance, and negligible for signals close to either reference. The estimates in Table II should be considered "worst-case."

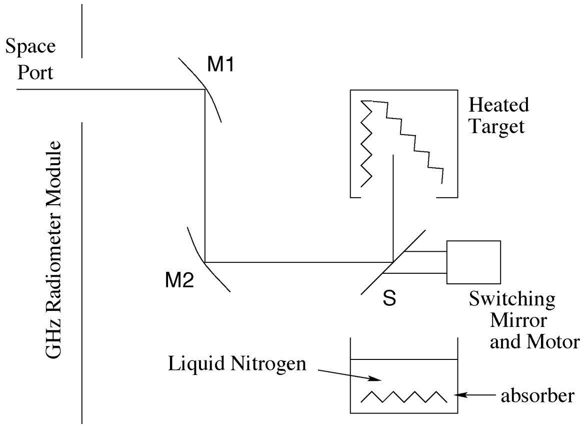

Fig. 2. This schematic illustrates the configuration to verify end-to-end linearity of MLS signal chairs.

III. Radiometric Calibration

Prelaunch radiometric calibrations consisted of the determination of calibration target emissivities and switching mirror baffle transmissions [3], and verification of linearity and noise performance. Fig. 2 illustrates the setup used to verify linearity of the GHz radiometers. Focusing mirrors M1 and M2 direct the view from the GHz radiometer space port to external switching Mirror S, which in turn directs the receiver FOVs toward either a liquid nitrogen (LN_2) cooled or a heated calibration target. The internal GHz module switching mirror additionally provides a view to either of the calibration targets in the radiometer assembly. The external heated target temperature can be varied between ambient and 100 °C, and its controller provides excellent stability. This target is a spare UARS MLS calibration load very similar to the internal Aura MLS ones, mounted in an insulated enclosure, with strip heaters on the aluminum backing plates of the absorbing surfaces, and platinum resistance sensors to both control and monitor target temperature. The LN_2 target consisted of a circular panel of grooved microwave absorber at the bottom of a stainless steel dewar. Standing waves in the views to the external targets were a few tenths of a Kelvin.

Fig. 3 is a picture of the linearity measurement setup. The instrument GHz module is mounted with the space port pointing down. Mirror M1, mounted below the space port, redirects the receiver FOVs horizontally toward M2. Switching mirror S is shown directing the FOV into the LN_2 dewar. The heated target

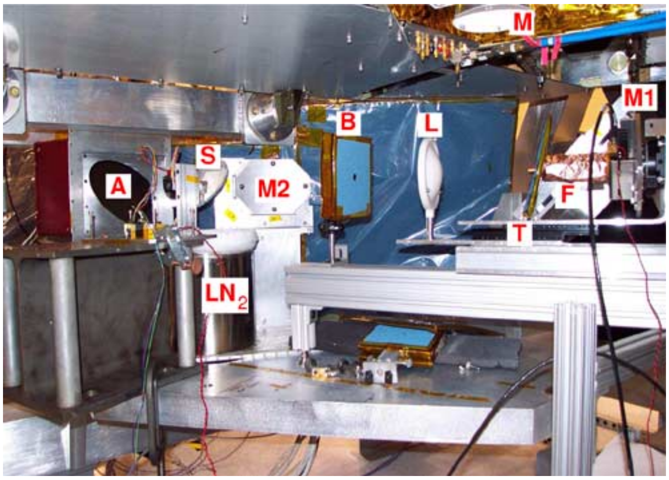

Fig. 3. Radiometric linearity and high-resolution spectral sweep calibration setup. See text for additional details.

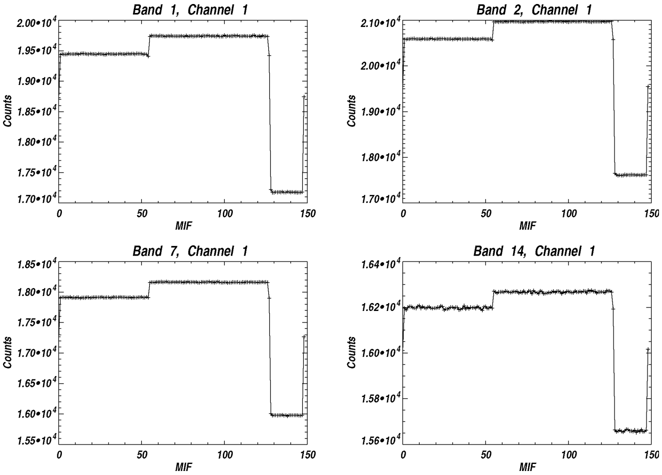

Fig. 4. Raw data for 1 MAF taken during a linearity measurement test. The four panels are data from individual 96-MHz filter channels in each of the GHz radiometers.

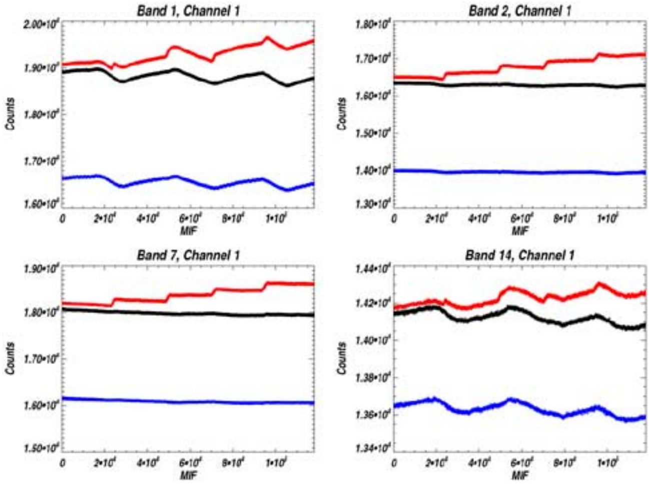

Fig. 5. Data as Fig. 4 for an entire linearity measurement run. The blue/black/red data are for the LN_2/ambient/heated target views respectively, each plotted point being a MAF-average. Note the cyclic drifts in these data.

aperture, A, is visible to the left of mirror S. The additional elements labeled in the figure are part of the spectral sweep setup discussed later.

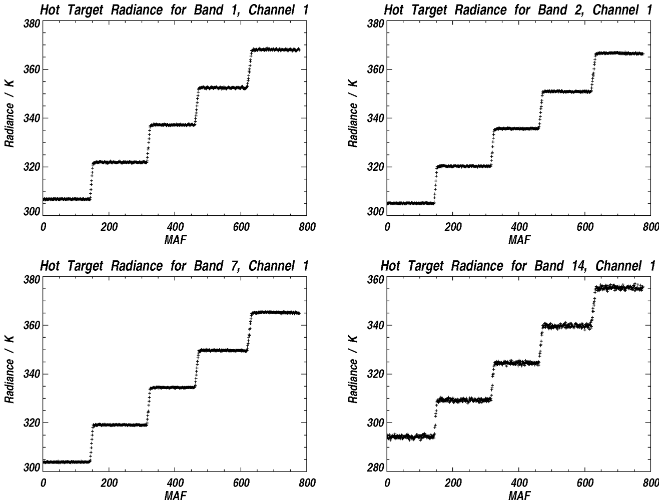

Fig. 6. Data of Fig. 5 processed by Level 1 software into heated target radiances. Note the removal of all instrumental drift-related artifacts.

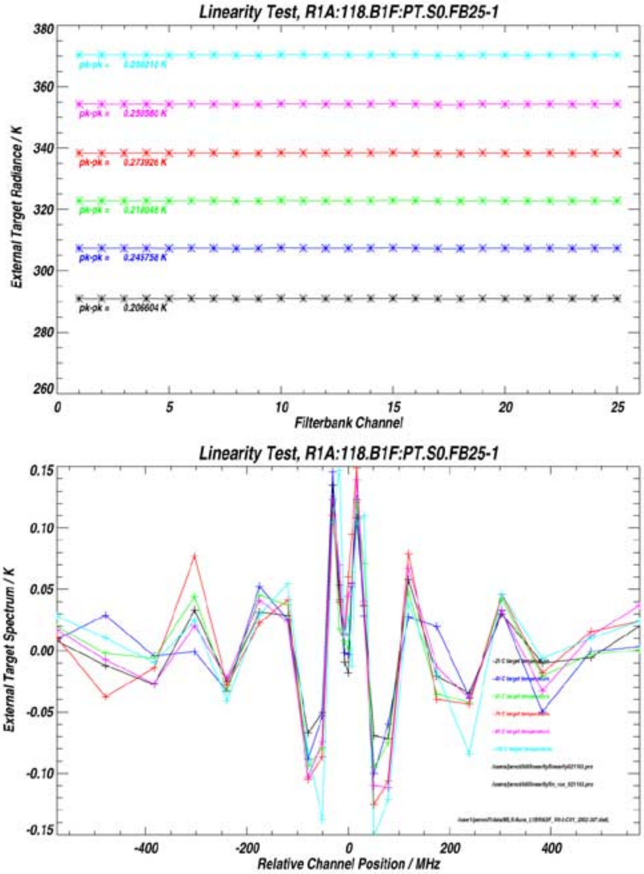

Fig. 7. Hot target radiances for all 25 channels of Band 1 (118-GHz radiometer) for six target temperatures ranging from room temperature to 100 °C. The lower panel shows the data from the upper panel with the band mean radiance subtracted from each measurement group.

Instrument linearity was measured using the three-point observing sequence ambient/heated/LN_2 targets. Operation of the external switching mirror was synchronized to instrument data integrations, allowing use of standard Level 1 software to convert these data into calibrated scene radiances. This avoided the need to write unique radiometric calibration software for this

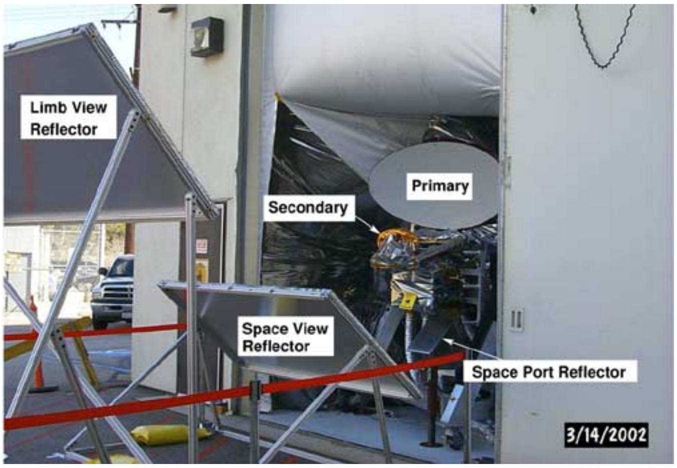

Fig. 8.“Blue Sky” measurement setup. See text for details.

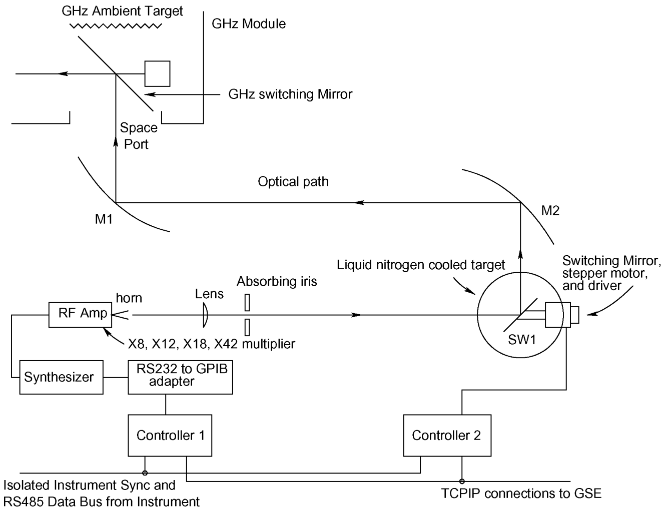

Fig. 9. Schematic of high-resolution front-end sweep setup.

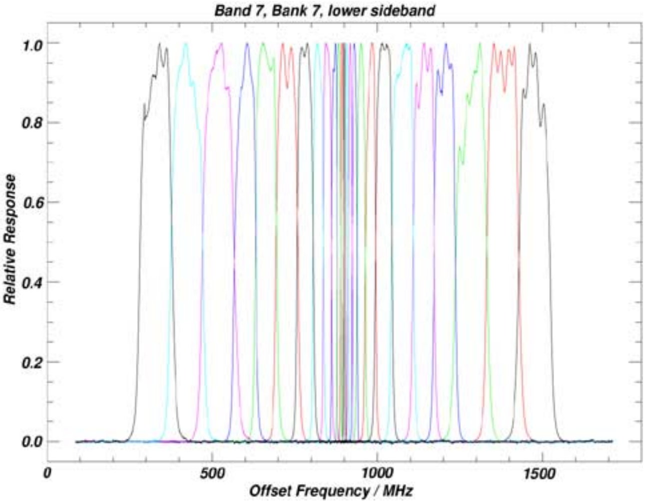

Fig. 10. Front-end sweep of the upper sideband of Band 7. The x axis is the spectrometer input frequency. All channels have been independently normalized to unity peak response.

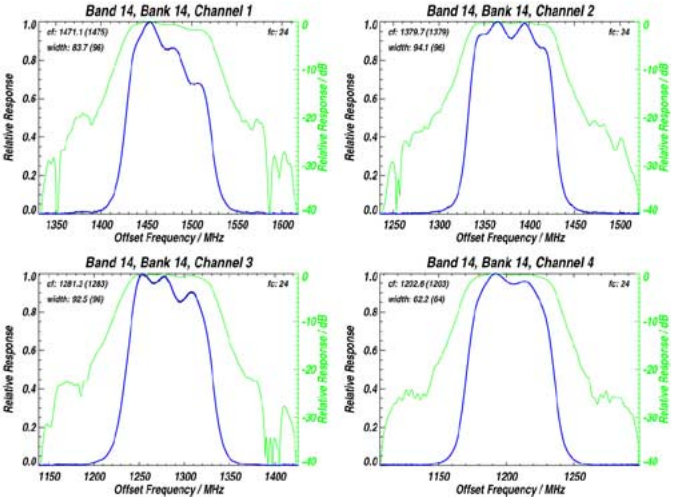

Fig. 11. End-to-end frequency responses of the first four channels in the upper sideband of Band 14 of R4. The responses are plotted on a linear scale in blue, logarithmically in green.

task while providing a valuable prelaunch validation of operational software with real instrument data.

An example of the raw data from 1 MAF during a linearity test run is shown in Fig. 4. The views to the three scenes are clearly visible. This measurement cycle was repeated with the heated target elevated in temperature in ~ 15 °C steps, with $\sim$45 min of stable data taken at each temperature plateau. Fig. 5 shows the same data for entire test, and the effects of gain and offset drifts are clearly visible. The same data are shown in Fig. 6 after processing by Level 1 software, showing the effective gain and offset drift compensation of the radiometric calibration algorithms.

1) Integral and Differential Linearity: Fig. 7 shows the individual channel data for R1A (the primary 118-GHz radiometer). In the upper panel the measured radiance at each target temperature is shown. The lower panel is the same data with the band mean radiance subtracted. Standing waves are clearly visible, and are present at similar levels in the data from all bands. The varying channel bandwidths and spacings within the MLS spectrometers complicate interpretation of the standing wave spectra, but analysis of data from all of the spectrometers indicates that the standing waves are consistent with reflections from the internal and external targets.

The majority of MLS measurements provide most of their information in the form of spectral contrast rather than absolute radiance in a given channel. For these measurements of most importance is the *difference* between the plots at different scene temperatures, since this a direct indication of differential linearity, or channel-to-channel breakup for out-of-balance scenes. The baseline correction at Level 1 effectively removes the effect of standing waves for measurements near radiometric balance with cold space. With UARS MLS we have measured clean H_2O_2 spectra with channel-to-channel differences of 0.001 K, a factor 10^6 below T_{sys}, as shown in [9, Fig. 12]. Standing waves similar in magnitude to those in the lower panel of Fig. 7 exist in the space-target differences for EOS MLS, not corrected in the current software, are the source of the 0.1% standing wave systematic error contribution in Table II.

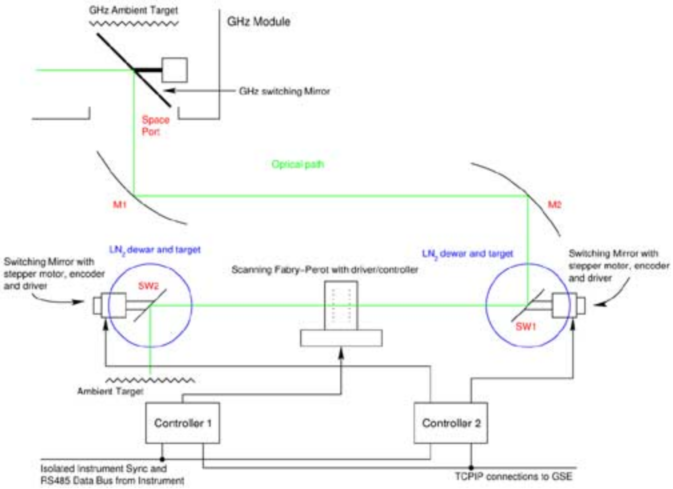

Fig. 12. Schematic of the Fabry–Perot sweep system used to measure relative sideband response in the GHz radiometers.

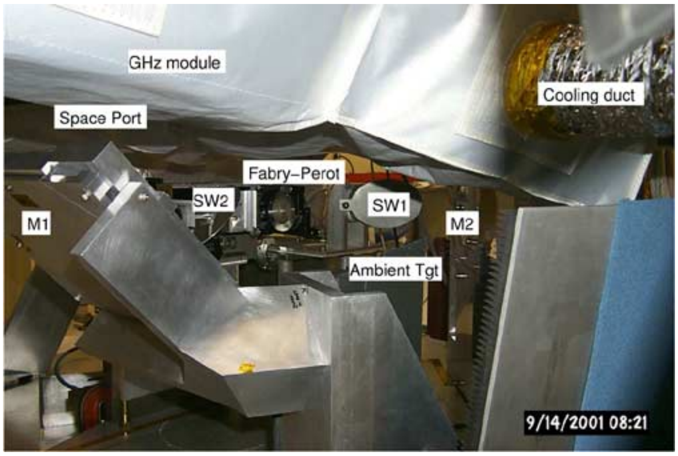

Fig. 13. Photograph of the Fabry–Perot sweep system depicted in Fig. 12.

Certain MLS measurements, notably those of water vapor and clouds, rely upon accurate determination of absolute limb radiances over large bandwidths. For such measurements good integral linearity is essential, and can be estimated by plotting band-averaged radiances versus scene temperature. Linearity measurements have been extended with data from in-flight tests using switching sequences that view both GHz calibration targets. Extrapolating these data indicate that we can place an upper limit of 0.1% on linearity error over the full dynamic range of atmospheric signals measured by MLS.

This outstanding linearity performance was obtained by running all RF amplifiers at least 12 dB below their 1-dB compression points, and operating all filterbank detector diodes with input power levels of −29 dBm or less. The ability to integrate signals down to levels well below the resolution of an individual measurement is obtained by appropriate design of postdetector digitizers. For both UARS and EOS MLS the digitizers are implemented as voltage-to-frequency converters (VFC) operating over a small portion of their dynamic range.

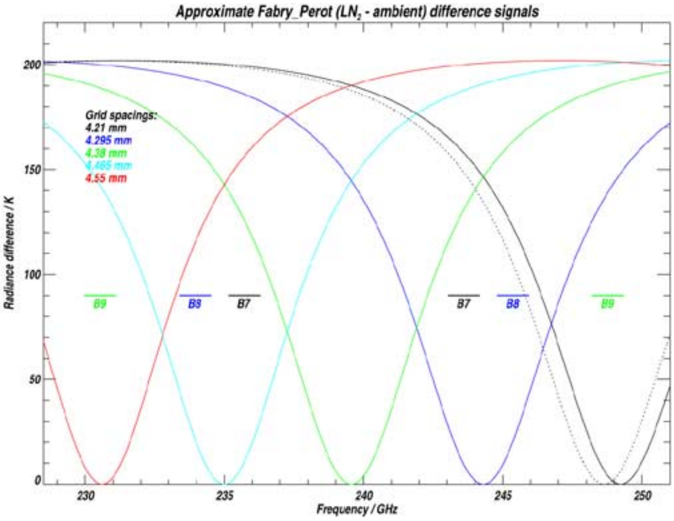

Fig. 14. Computed radiance signatures generated by the Fabry–Perot when sweeping the 240-GHz radiometer bands. The dashed line shows the spectral shift corresponding to a 0.01-mm increase in grid spacing from the initial spacing. Band positions in both sidebands are indicated for reference.

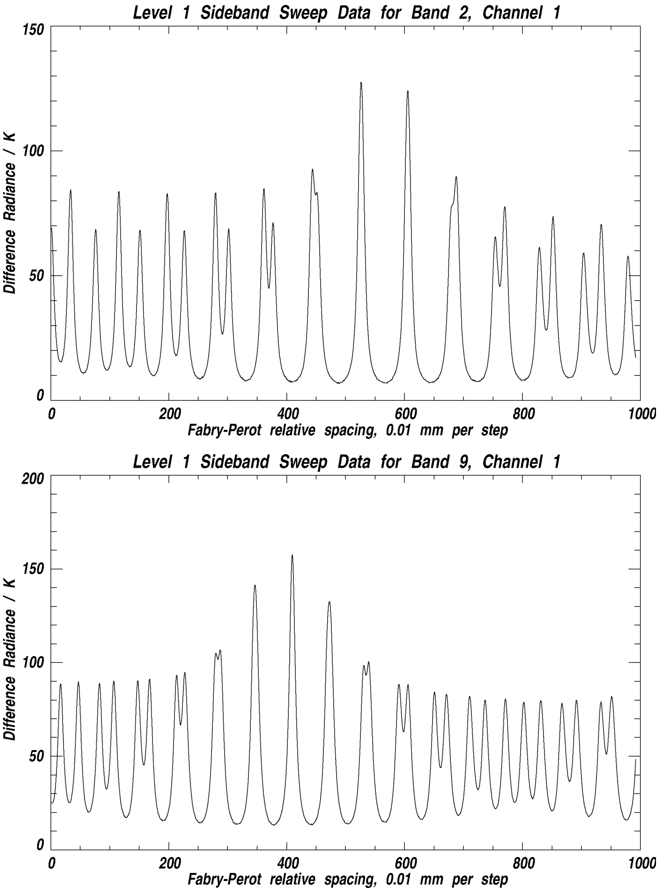

Fig. 15. Level 1 radiances from channel 1 of band 2 (upper) and band 9 (lower) as the Fabry–Perot grid spacing stepped from ∼3.74 to ∼9.93 mm. These data were taken concurrently. Grid step size was 0.01 mm for sweeps of the 190- and 240-GHz bands.

A. Additional Performance Tests

In addition to linearity measurements, tests were run to investigate radiometric sensitivity. The ability to integrate down the noise on data from scenes at temperatures very different from

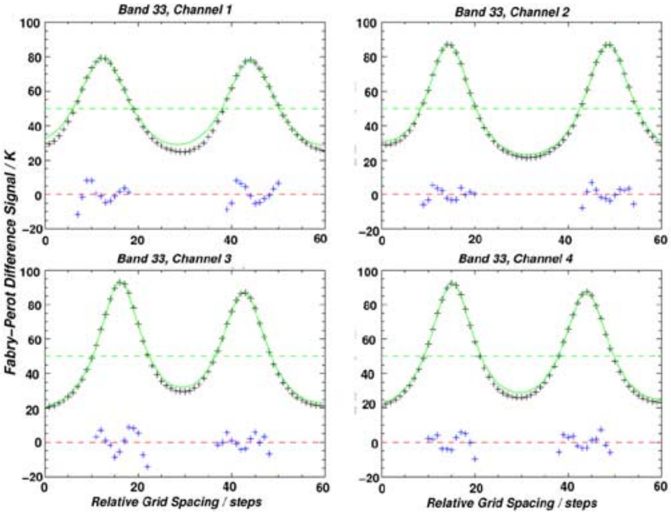

Fig. 16. Plot showing measured (crosses) and modeled (green line) Fabry–Perot signals for the four wide filter channels in the 240-GHz radiometer. Each grid spacing step corresponds to an increase in grid separation of 0.01 mm. The blue crosses show the differences between measurement and model, inflated by a factor of 10.

the radiometers was verified from a 12-h data set taken with the GHz module switching between limb and space ports, and the FOVs of both limb and space ports directed by plane mirrors into LN_2 loads of the type shown in Fig. 3. This test was run when the GHz radiometer module was not integrated with the main antenna. In addition to the limb and space port views, a short view to the internal GHz ambient target was performed during each MAF in order to determine channel gain. Results from this test indicated consistency in the data from both target views down to the ∼20-mK level in all bands.

An end-to-end test (the "Blue Sky" test) was run in which the complete instrument was located at the air lock to the assembly building, oriented in such a manner that two large plane aluminum faced panels could be used to direct the FOVs of both antenna and space port near zenith (Fig. 8). The signal levels at the two ports were balanced by adjusting the angle of the lower panel, and multihour data sets taken while switching between the two internal calibration targets and the space and limb ports. For this test one of the internal targets was heated by ∼25 °C to enable the data processing software to continuously determine channel radiometric gain.

A key goal of this test was to verify the absence of any scan-dependence of the spectral baseline signature. This is of crucial importance, since we rely on the baseline signature measured at high tangent heights to correct the data taken looking lower in the atmosphere. Data were taken with the antenna actuator at its nominal and extreme positions, well beyond the range of scan angles used operationally. The spectral differences between these data sets indicated no scan dependence down to the noise level of the measurements, ∼20–40 mK. An unexpected result from the data taken in this test was that it revealed a subtle performance problem with the spectrometer power system which had to be corrected by the addition of multiple regulators to each spectrometer chassis. Further details of the measurements and results are in [10].

IV. SPECTRAL CALIBRATION—HIGH RESOLUTION

All GHz channels were swept using synthesized fundamental sources coupled into the space port of the GHz radiometer module. Channel responses were measured at approximately 100 uniformly spaced points, with the sweeps extending substantially beyond the nominal filterbank bandpasses to capture any extraneous responses. Sweeps were performed in both sidebands (except for the single-sideband 118-GHz receivers), and with all combinations of switch network settings. The measurement setup is the one shown earlier in Fig. 3. The GHz module (M) space port is directed vertically down toward focusing mirror $\mathsf{M1}$, seen edge on in the figure. Mirror $\mathsf{M2}$ directs the instrument FOV toward switching mirror S which is shown pointing toward the LN_2-cooled target in dewar $\mathsf{LN2}$. During active sweeps S directs the instrument FOV through the small hole visible in absorbing baffle B, through lens L, and finally onto the small horn visible at the left hand end of fundamental source F. A schematic of the sweep setup is shown in Fig. 9.

A. Signal Sources

A family of signal sources, F, were used to span the 114–662-GHz range covered by the GHz receivers. A single source covered all of the bands in a given receiver, and all sources were fed by a programmable synthesizer operating in the 13.5–17.1-GHz range. The sources multiplied the synthesizer output frequency by factors of 8, 12, 18, or 42 depending upon the band/sideband being swept. The small fractional bandwidth of each channel ensured that the power from the source remained constant over the width of a channel. Minor problems were encountered sweeping a handful of channels when unwanted harmonics from the multiplier passed through the channel response in the opposite sideband to the one being targeted. There were also some instances where the mode of an unused harmonic in the source jumped, causing a small change in RF power. Both of these conditions were readily identifiable in the data, and fixes were built into the analysis software to correct these potential error sources [10].

B. Standing Waves

With the 118-GHz radiometers it was observed that the relatively large iris aperture in B needed for these sweeps, combined with the precise optical alignment between test equipment and receivers, created noticeable standing waves. These were readily observed by performing a sweep of a 96-MHz channel twice, with the source moved by $\lambda/4$ between sweeps. It became standard practice to check for standing waves, and perform a pair of $\lambda/4$ separated sweeps for afflicted bands. The analysis software then combined these data so as to remove the effects of the standing waves. To make precision adjustment of the source location easy and repeatable, it was mounted on a micrometer-driven translation stage. The source was mounted on a rotation stage for ready alignment of the polarizations of source and receiver.

C. Results

Fig. 10 shows the results of an upper sideband sweep of Band 7 of R3, covering a frequency range of ∼242.7 to 244.4 GHz.

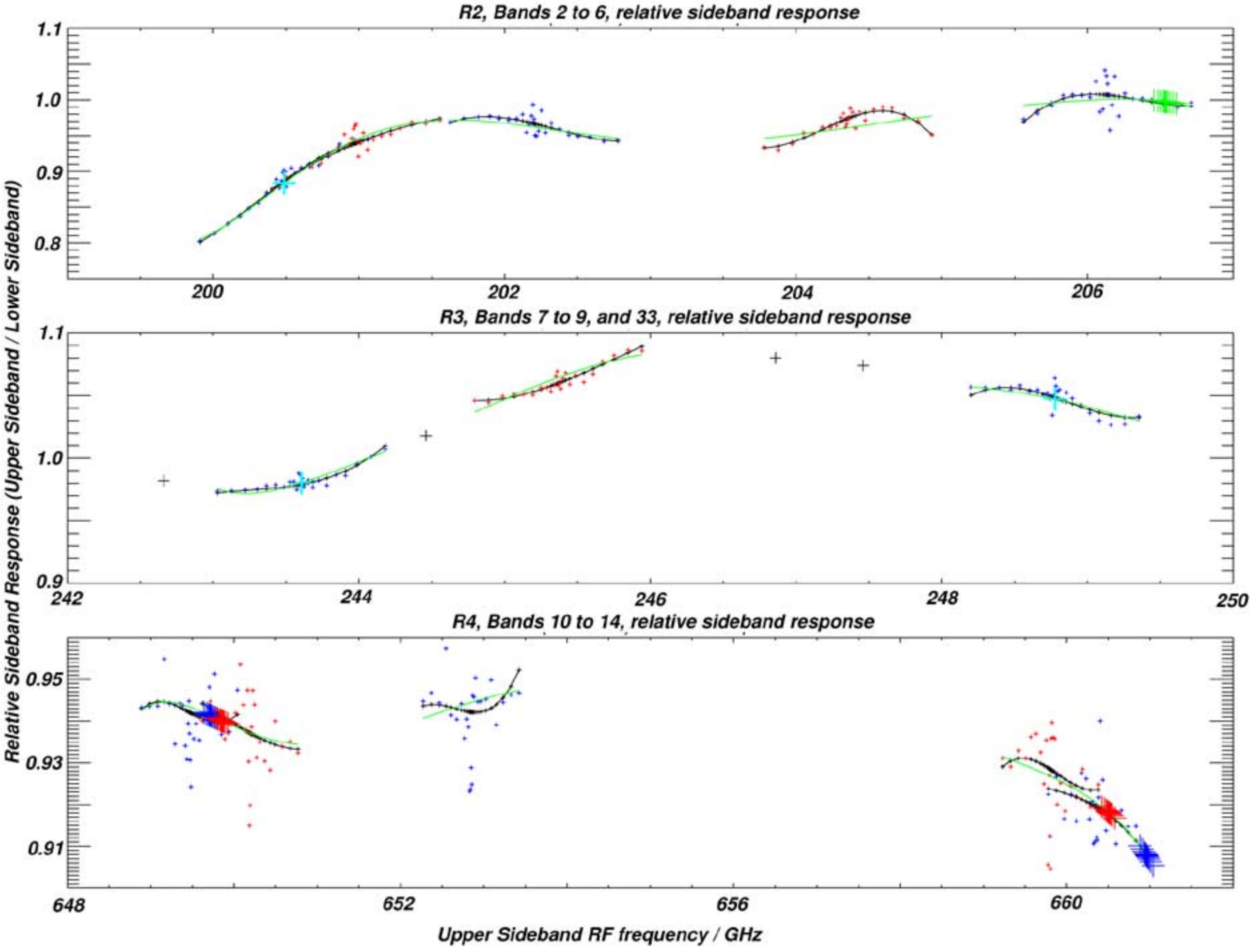

Fig. 17. Relative sideband response for all double sideband channels of the GHz radiometers. The large plus signs in the center panel are sideband data for the wide filter channels in R3. The large green, red, and blue plus signs in the other panels are the sideband responses in the midband filterbanks (bands 27 to 31). Black line segments are results of sideband retrievals on individual bands, and the green segments are a global fit to these data for all bands in a given radiometer. Individual small red and blue plus signs are from sideband retrievals performed on individual channels.

The plot was made with the "quick look" tools used to verify data quality in near real time. Fig. 11 shows the detailed responses of the highest frequency FB25 channels in the GHz module.

V. SPECTRAL CALIBRATION—LOW RESOLUTION

In a double-sideband measurement system like EOS MLS it is necessary to determine the *relative* response of each channel in the two sidebands. We measured relative sideband response by observing the difference between ambient and LN_2 loads viewed through a scanning Fabry–Perot interferometer. A schematic of this setup is shown in Fig. 12, and a photograph in Fig. 13. This setup uses two external switching mirrors. The first one (SW1) directs the receiver FOVs to either an LN_2 load or the Fabry-Perot. The second (SW2) directs the FOV through the Fabry–Perot to either ambient or LN_2 loads. The internal GHz switching mirror directs the FOVs to either an internal ambient load or the external calibration setup.

A family of calculated Fabry–Perot transmission curves is shown in Fig. 14 for the 240-GHz radiometer using 90-line/inch (lpi) grids. The widths of the transmission orders are seen to be considerably wider than the individual bands being characterized. The orders of the Fabry–Perot are seen to be well separated in all bands in this example. Sweeps of the 640-GHz radiometer bands were performed with finer (200 lpi) Fabry–Perot grids and smaller grid spacing step size (0.002 mm), resulting in raw data looking very similar to that shown in Fig. 15. Sweeps with both grid sets were performed over large enough ranges of grid separations that the sideband responses of all bands were well resolved over several Fabry–Perot orders.

A. Analysis and Results

Sideband sweep data from the lowest and highest frequency double sideband channels swept using the 90-lpi grids, after conversion into equivalent brightness temperatures, is shown in Fig. 15. The sweep data for the 640-GHz bands, taken using 200-lpi grids and smaller grid separation steps, look similar.

These data were fit on a per-band basis using a conventional formulation for the Fabry–Perot transmission [11]. Model parameters included relative sideband response, upper and lower sideband grid reflectivities, and initial grid separation. An example of measured and modeled data for the wide filter channels of the 240-GHz radiometer is shown in Fig. 16.

The relative sideband data for all double sideband GHz bands are shown in Fig. 17. Fits to individual 25-channel filterbank bands (FB25) are indicated by the black curve segments, where channel positions are indicated by the small plus signs. The small red and blue plus signs are the results from performing relative sideband retrievals on the data from individual channels, shown for information. Since there is overlap in several bands, and relative sideband response is defined by the front-end receiver, we chose to perform a global fit to all of the FB25 sideband data in a given radiometer. This defines sideband response as a unique function of IF frequency, and the results of these fits are shown by the green lines, which are the data used by the forward model [12] in the Level 2 software [13]. The large green, red, and blue plus signs indicate the inferred sideband responses in the 11-channel filterbank bands (FB11), and the large plus signs in the center panel are sideband responses for the wide filter channels in R3, which were retrieved on a channel-by-channel basis. Additional details of the sideband calibration setup, including its alignment, measurement timing, and data analysis, are given in [10].

B. R4 Sideband Response

After delivery of the MLS instrument for integration on the Aura spacecraft, the whisker-contacted tripler in the first LO source for R4 was replaced by a more robust one using planar diode technology. The R4 receiver front-end was removed and returned to JPL for this rework. One consequence of this change to the receiver was a small change in LO drive level and matching, resulting in a small but significant change in relative sideband response. Since the end-to-end signal chains were not available at this time, the sideband response of the receiver was measured with a simplified Fabry–Perot and IF/filter setup before and after the tripler changeout. These measurements indicated a change of ~4%, and calibration data files used by Level 2 processing were updated accordingly.

VI. MASTER OSCILLATOR

All critical frequencies sources in the MLS instrument are referenced to a 5-MHz Master Oscillator (MO). Trend data taken over a ~480-day interval prior to instrument launch is shown in Fig. 18 for both the primary and backup units. The requirement is for drift of no more than 1 part in 7×10^{-8} of the starting frequency at the end of the mission (six years after launch), corresponding to 0.35 Hz. Extrapolation of the data in the figure indicates that requirements will be met. In-orbit spectra observed by the digital autocorrelators (DACS) provide a very sensitive measure of first LO placements in R1 and R3, and provide a valuable indicator that no unexpected shift or drift has taken place in the MO frequency during the first year of in-orbit operation.

VII. SPECTRAL CALIBRATION ACCURACY

Requirements on spectral calibration accuracy are similar to those for radiometric calibrations, and may be summarized as: the systematic error contribution in calibrated radiances shall be no more than 1% of the calibrated scene radiance. This allocation is separately applied to high-resolution and relative sideband data.

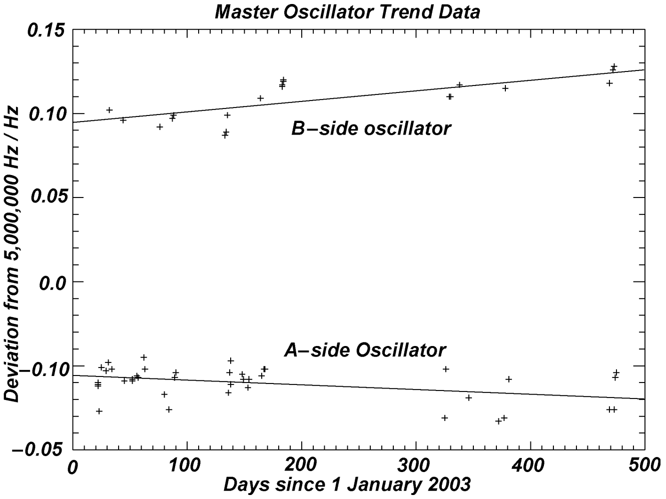

Fig. 18. Trend plot showing prelaunch drifts of the primary (lower) and backup master oscillator frequencies.

For the high-resolution sweep data the most sensitive parameter is channel position, and since all downconversions are locked to the ultra-stable MO, we anticipate no frequency drifts in the signal chains that precede the spectrometers. The DACS process their input signals digitally, and are similarly immune to drifts. The only likely potential source of significant channel drift arises in the *LC* filters used to define the bandpasses of each filter spectrometer channel. The spectrometers were extensively temperature-cycled before instrument delivery, and no evidence of channel drift was detected. An on-board synthesizer, which uses the MO as its reference, can determine filter characteristics in flight should the need arise. Level 2 residuals to date give no indication of any drifts.

The end-to-end sweeps of channel position/shape were of very high precision as evidenced by the sample data shown in Fig. 11, making shape errors also a negligible source of error. A potential error source in these measurements arises from “out of band” responses which could be at a low level compared to the peak response of any channel, but could also span a much larger frequency range than the nominal filter width. No such responses were observed in either high- or low-resolution sweep data, but to be conservative we have chosen to allow the error budget for filter channel position and shape to be 0.3% of the measured radiance.

The uncertainty in relative sideband response is difficult to estimate. For the 118-GHz radiometers their single sideband response was adequately verified by front-end sweeps in the image sideband using a fundamental source, and by examination of the 90-lpi Fabry–Perot sweep data. For relative sideband responses close to unity, the case for all of the GHz double-sideband MLS radiometers, a fractional error of δ translates into a corresponding radiance error of $\delta/2$ in each sideband.

For R2 the largest deviations between the individual band and IF-wide fit data are ~0.02 in relative sideband response, corresponding to 1% error in single sideband radiance. For R3 the errors are approximately half as large, and for R4 half as large again, indicating peak relative sideband uncertainties of ~0.01 and ~0.005, corresponding to radiometric errors of 0.5% and

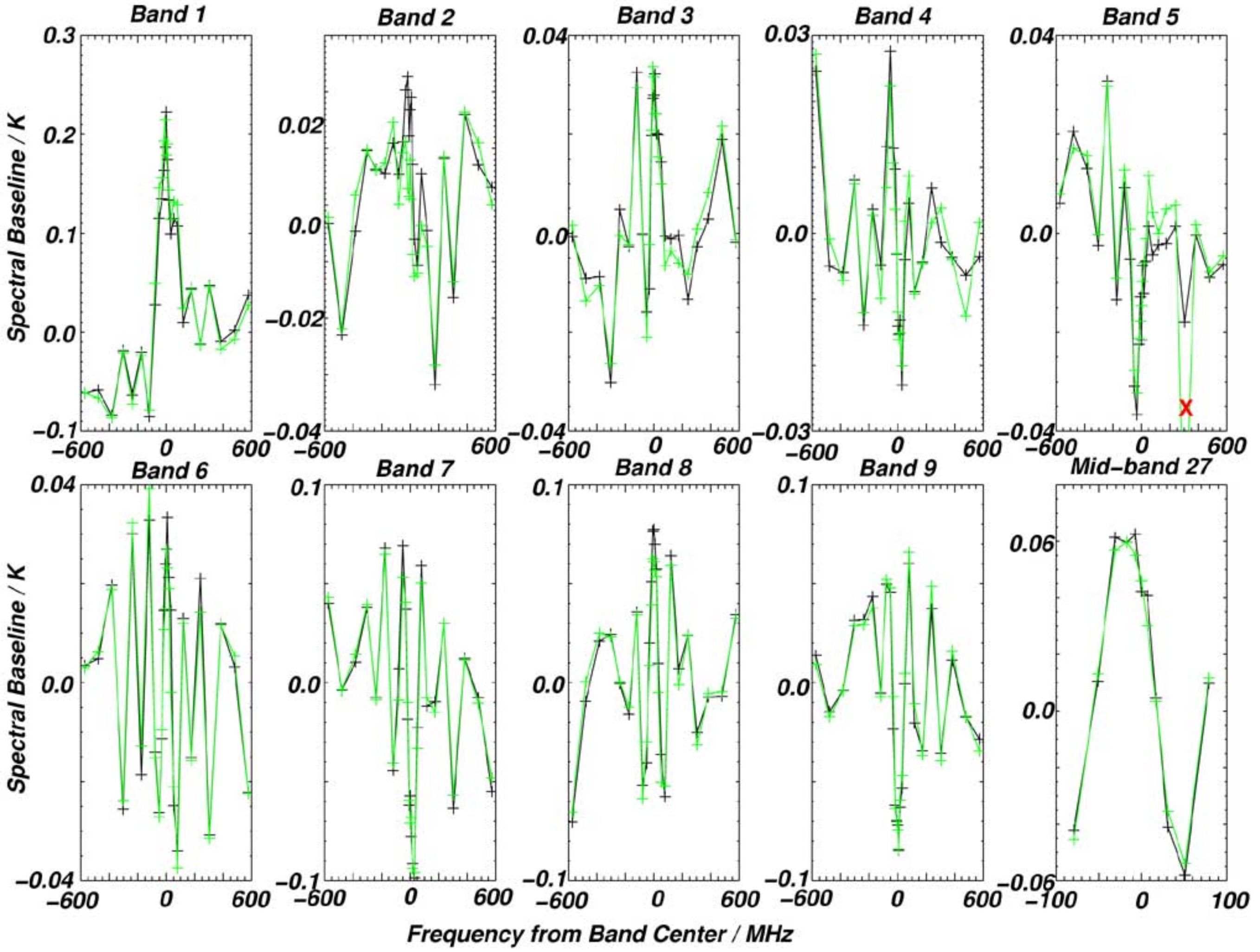

Fig. 19. Spectral baseline plots for filter bands in the 118-, 190-, and 240-GHz radiometers. The black data are for tangent points from ∼250 and ∼300 km, the green data for tangent points between ∼120 and ∼170 km. The red cross in Band 5 indicates a channel subject to internally generated interference.

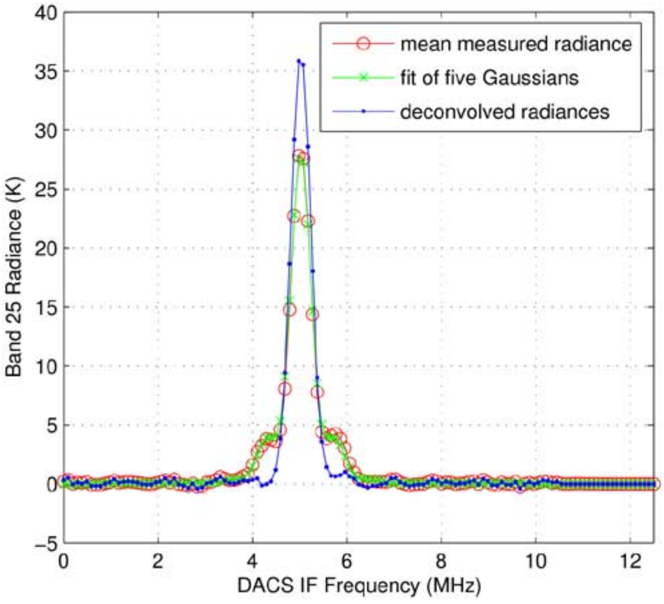

Fig. 20. CO spectrum from B25, before and after correction for first LO spurs.

0.25% in these radiometers. The presence of unidentified systematics in these measurements may result in these uncertainty estimates being slightly optimistic, but even so it is reasonable to assume that the combination of errors in high-resolution and relative sideband calibration data comfortably meet the intent of the requirements. We assume that sideband uncertainties correspond to errors in double-sideband calibrated radiance of 0.3% in R1 (single sideband for this radiometer), 0.8% in R2, and 0.55% in R3 and R4.

VIII. IN-ORBIT PERFORMANCE

In-orbit performance of the GHz radiometers is very close to that observed during ground testing, but with improved $1/f$ characteristics due to the more benign thermal environment and lack of convection-induced artifacts.

IX. IN-ORBIT CALIBRATION

The most significant in-orbit calibrations are refinement of pointing knowledge through moon scans, updates to antenna scattering, emission and ohmic loss parameters, and determination of spectral baseline. These updates were expected based on prior UARS MLS experience, and are described in more detail in [3] and [10]. An unexpected in-orbit calibration update arose because of the presence of 1st. local oscillator spurs in the 240-GHz (R3) radiometer. These were known to be present prior to launch, but the optical bench temperature in flight was raised using operational heaters to reduce the spectrally varying noise in the 640-GHz radiometer, resulting in the spurs being at a higher than anticipated level. Baseline performance and spur compensation are discussed below.

Possible future in-orbit calibrations include the use of saturated atmospheric radiances to validate/refine relative sideband ratio knowledge, and also the development of methods for reducing the effects of standing waves in the views to the calibration loads, and for tracking changes in antenna spectral baseline.

A. Spectral Baseline

Proof that spectral baseline signatures are stable can only come from analyzes of in-flight data. In order to observe scan dependence of spectral baseline the antenna was scanned between tangent heights of 120 km and 300 km, well above the altitudes at which we expect to see significant atmospheric signals, and approximately twice the angular range exercised in a routine atmospheric limb scan. The data from these measurements is shown in Fig. 19, with band-average radiances removed so that the data overlay. The black spectra are for views with tangent heights between ∼250 and ∼300 km, the green spectra for views between ∼120 and ∼170 km. The lack of scan dependence of spectral baseline is evidenced by the very small differences between the black and green plots. The spectral feature in the data for Band 5 marked with a red cross is from a channel subject to internally generated interference, and which is not used in higher levels of data processing. Spectral baselines in the 640-GHz bands are ∼0.05 K *pk-pk*, but they are not persistent in time, and are further reduced by the long-term data averages needed for weak signals.

Just as important as the lack of scan-dependence for spectral baseline is its long-term stability. Spectral baseline has been measured several times during the mission, at different seasons (i.e., different solar β angles), and with the internal operational heaters both off and fully on. These data indicate a maximum variation in spectral baseline during the first year of operation of ∼30 mK. We are currently determining the feasibility of accounting for this time dependence by estimating spectral baseline on a daily basis, as was done for UARS MLS.

B. R3 Spur Compensation

An unexpected behavior observed in flight was the presence of varying spurs in the R3 first LO, which manifested as clear artifacts in the DACS data radiance residuals. The presence of these spurs was known before launch, but they were expected to be stable. These spurs are offset ±714 kHz from the LO fundamental frequency. There is a second, much smaller, pair of spurs at ±1428 kHz. During the first six months of MLS operation the fraction of LO power in the spurs has ranged from less than 15% to more than 36%, with large changes associated with relatively small changes in operating conditions that effect the temperature of RF components.

As a result, Level 1 software has been modified to estimate the magnitude of spurs, and the spectra are corrected for their effects, as shown in Fig. 20. Estimates are made separately for B24 and B25 (DACS bands 24 and 25) to simplify handling of missing data, even though the underlying source is the R3 LO in both cases. The spur amplitudes are retrieved from daily mean, high-altitude (tangent point above 78 km) spectra from B24 and B25, which contain multiple images of the Doppler-broadened 235-GHz O_3 line and 230-GHz CO line, respectively. All measured atmospheric spectra are divided by the discrete cosine transform of the retrieved LO shape in the Fourier domain to effectively deconvolve the LO shape from the spectra, and the estimated measurement precisions are updated accordingly. Further details are given in [6].

X. CONCLUSION

This paper has described the radiometric performance, and radiometric and spectral calibrations of the GHz component of Aura MLS. All performance and calibration requirements have been met, and, as with its UARS predecessor, we expect instrument calibration to be maintained, and in some areas enhanced, during the mission.

ACKNOWLEDGMENT

Numerous people contributed to the success and efficiency of the prelaunch characterization and calibration activities, including R. Cofield for designing and providing the external optics for the calibration setups, and more importantly, the means to rapidly align them; M. Loo, J. Garcia, G. Melgar, and J. Holden for operating the instrument during calibrations; D. Benson and P. Vosse for fabricating the many brackets and supports crucial to the calibration setups; K. Lee and K. Chandra for their support of the spectral sweeps; T. Crawford for providing the grid holders used in sideband sweeps; and J. Waters for having faith in the aggressive schedule for this activity. Many other colleagues, too numerous to mention here, made valuable contribution to this effort, and the authors wish to thank them all.

REFERENCES

[1] F. T. Barath *et al.*, “The Upper Atmosphere Research Satellite Microwave Limb Sounder instrument,” *J. Geophys. Res.*, vol. 98, pp. 10751–10762, 1993.

[2] J. W. Waters *et al.*, “The Earth Observing System Microwave Limb Sounder (EOS MLS) on the Aura satellite,” *IEEE Trans. Geosci. Remote Sens.*, vol. 44, no. 5, pp. 1075–1092, May 2006.

[3] R. E. Cofield and P. C. Stek, “Design and field-of-view calibration of 114–660-GHz optics of the Earth Observing System Microwave Limb Sounder,” *IEEE Trans. Geosci. Remote Sens.*, vol. 44, no. 5, pp. 1166–1181, May 2006.

[4] H. M. Pickett, “Microwave Limb Sounder THz module on Aura,” *IEEE Trans. Geosci. Remote Sens.*, vol. 44, no. 5, pp. 1122–1130, May 2006.

[5] R. F. Jarnot, R. E. Cofield, J. W. Waters, and D. E. Flower, “Calibration of the Microwave Limb Sounder on the Upper Atmosphere Research Satellite,” *J. Geophys. Res.*, vol. 101, no. D6, pp. 9957–9982, Apr. 1996.

[6] R. F. Jarnot, H. M. Pickett, and M. J. Schwartz, “EOS MLS Level 1 data processing algorithm theoretical basis,” JPL, Pasadena, CA, Tech. Rep. JPL D-15210.

[7] F. N. H. Robinson, *Noise and Fluctuations in Electronic Devices and Circuits*. Oxford, U.K.: Clarendon, 1974, ch. 19.

[8] J. W. Waters and R. F. Jarnot, “Sciencey requirements on the EOS MLS instrument and data processing software,” JPL, Pasadena, CA, Tech. Rep. JPL D-14421, Rev. 3, Feb. 26, 2002.

[9] J. W. Waters, “Observations for chemistry (remote sensing): Microwave,” in *Encyclopedia of Atmospheric Sciences*, J. Holton, J. Curry, and J. Pyle, Eds. New York: Academic, 2003, pp. 1516–1528.

[10] R. F. Jarnot, R. E. Cofield, H. M. Pickett, and P. C. Stek, "EOS MLS instrument calibration report," JPL, Pasadena, CA, D-26280, 2006, to be published.

[11] M. Born and E. Wolf, *Principles of Optics*, 6th ed. New York: Pergamon, p. 329.

[12] W. G. Read *et al.*, "The clear-sky unpolarized forward model for the EOS Aura Microwave Limb Sounder (MLS)," *IEEE Trans. Geosci. Remote Sens.*, vol. 44, no. 5, pp. 1367–1379, May 2006.

[13] N. J. Livesey *et al.*, "Retrieval algorithms for the EOS Microwave Limb Sounder (MLS)," *IEEE Trans. Geosci. Remote Sens.*, vol. 44, no. 5, pp. 1144–1155, May 2006.

Robert F. Jarnot received the Dr.Phil. degree in atmospheric physics from Oxford University, Oxford, U.K., in 1977, during which time he made the first stratospheric NO measurements using a balloon-based infrared pressure modulator radiometer.

Since then he has been with the Jet Propulsion Laboratory, California Institute of Technology, Pasadena, working on various incarnations of MLS instruments ranging from balloon- to satelliteborne versions. His roles have included C&DH, digitizer, analog data subsystem, and low-noise amplifier design, onboard and ground-based support and analysis software design and implementation, responsibility for Level 1 algorithms, instrument calibration, and general troubleshooting.

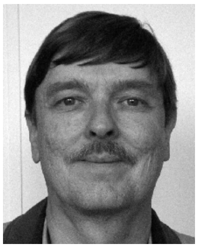

Vincent S. Perun studied physics and electrical engineering at Case Western Reserve University, Cleveland, OH.

In 1983, he joined the Jet Propulsion Laboratory, California Institute of Technology, Pasadena, to write software to support development and operation of the various MLS instruments. Responsibilities include Level 1 programming and data analysis tools.

Michael J. Schwartz began his undergraduate education at Deep Springs College, Deep Springs, CA. He received the B.A. degree in physics from Carleton College, Northfield, MN, and the Ph.D. degree in physics from the Massachusetts Institute of Technology (MIT), Cambridge, in 1985 and 1998, respectively. His thesis, supervised by Prof. D. H. Staelin, involved atmospheric remote sensing with millimeter-wave oxygen lines.

He was on the research staff of the MIT Research Laboratory of Electronics in 1999, where he contributed to the development of an aircraft-based atmospheric sounding package. In 2000, he joined the Microwave Limb Sounding Group at the Jet Propulsion Laboratory. His responsibilities included the development of digital autocorrelator spectrometer hardware and processing algorithms for the EOS-MLS instrument, oversight of the MLS temperature and geopotential height data products, and development of the polarized forward model for Zeeman-split oxygen lines.